Acta Astronautica 245 (2026) 416–429

Contents lists available at ScienceDirect

Acta Astronautica

journal homepage: www.elsevier.com/locate/actaastro

Research Paper

A comprehensive ground–flight testing approach for the dynamic performance of a critical space mechanism

E. Dalla Ricca [a,c,1], D. Bortoluzzi [a,c,*,1], D. Vignotto [b,c], M. Tomasi [a,c], A. Gelan [a,c]

[a] Department of Industrial Engineering, University of Trento, Via Sommarive 9, 38123, Trento, Italy
[b] Department of Physics, University of Trento, Via Sommarive 14, 38123, Trento, Italy
[c] National Institute for Nuclear Physics (INFN), TIFPA, Via Sommarive 14, 38123, Trento, Italy

ARTICLE INFO

Keywords:
Space mechanism
On-ground testing
In-flight testing
Mechanism dynamics
Release mechanism

ABSTRACT

On-ground testing of spacecraft is often a challenging task, including the design and development of dedicated setups, proper system modeling and data analysis techniques. However, sometimes ground-based testing may not be fully representative of the in-flight operation and a technology demonstration mission is flown to provide evidence of the maturity of critical technologies.

This is the case of LISA Pathfinder (LPF), technology demonstration mission for LISA. We deal here with the LISA core instrument, namely the Gravitational Reference Sensor (GRS), which was successfully tested on board LPF. The focus is on the mechanism in charge of providing the initialization of its scientific phase, the grabbing, positioning and release mechanism (GPRM). The GPRM injects a reference mass hosted in the GRS into a pure geodesic trajectory, realizing essentially a second mission launch in reduced scale, characterized by very tight requirements. A dedicated strategy is put in place to provide a ground-based test of this function, starting from the concept up to involving an engineering qualifying model of the mechanism and developing a customized test approach, data analysis and result synthesis methods. The mechanism operation on board LISA Pathfinder however resulted anomalous, producing an out-of-nominal state of the reference mass. As a consequence, part of the extended mission phase was dedicated to perform some testing of the injection phase, to find risk-reduction strategies and understand the root cause of the anomaly.

In this paper, we report on the result synthesis of the combined ground–flight testing campaign, proposing some mechanism development guidelines for LISA.

1. Introduction

Mechanisms often constitute critical subsystems of spacecraft, since their functionality and performance may severely affect the success of the mission [1]. As a consequence, their design, development and testing must guarantee that a near-absolute reliability is ensured in the mechanism flight configuration. This must be achieved by identifying and testing the mechanism according to global requirements. These requirements accurately address the general spacecraft environment, the launch phase, the spacecraft structure and the thermal behavior characterizing the operational conditions [2].

A spacecraft experiences different physical environments throughout its lifecycle, from construction and testing on Earth to launch and operation in space. On Earth, it is subject to 1-g acceleration, controlled temperature, and atmospheric conditions. During launch, it encounters high levels of vibration, acoustic noise, shocks, and heat flux. Once in orbit, operational conditions depend on the trajectory and are dominated by vacuum and radiation effects [1]. The most severe environmental conditions for a mechanism are experienced during launcher-specific qualification or acceptance tests. After that, the flight unit is subjected to flight acceptance tests, which are more representative of the actual launch condition. Conversely, in the operating conditions space mechanisms are mainly challenged in terms of material properties, tribological effects and thermal gradients [3].

Besides some standard requirements to be verified (life test, thermal cycling, motorization factor, wear, debris, etc.), tests assessing dynamic performance in operating conditions target different critical aspects depending on the specific mechanism. Deployment systems for antennas, booms, instruments, sails, etc. are tested for their dynamic response (induced shock) and stability of the deployed configuration.

* Corresponding author at: Department of Industrial Engineering, University of Trento, Via Sommarive 9, 38123, Trento, Italy.
E-mail address: daniele.bortoluzzi@unitn.it (D. Bortoluzzi).
[1] Equal first authors.

https://doi.org/10.1016/j.actaastro.2026.03.025
Received 24 September 2025; Received in revised form 9 February 2026; Accepted 8 March 2026
Available online 9 March 2026

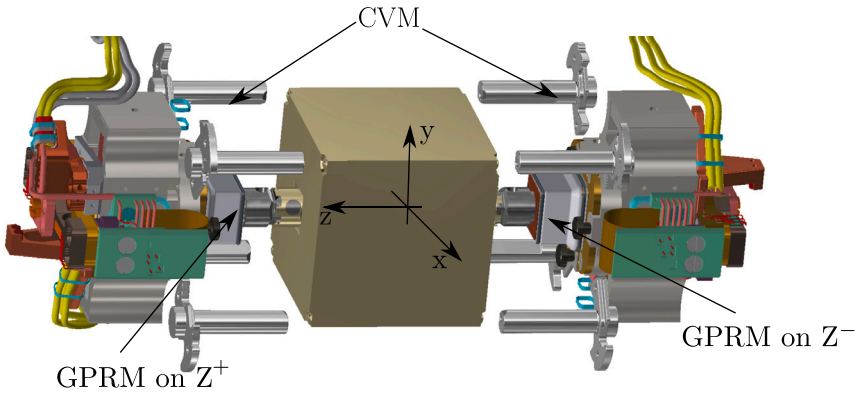

Fig. 1. TM reference system.

Reaction wheels and drive mechanisms are tested in terms of micro-vibrations induced on the spacecraft and subsequent jitter at the instrument payload [4]. Scan assemblies and pointing systems (for antennas, telescopes, propulsion systems, mirrors, solar arrays, etc.) are also tested for their pointing accuracy and stability. Launch lock devices, latching mechanisms and hold-down-release mechanisms are tested for the induced shock on the spacecraft, friction/adhesion/fretting at the contacting surfaces and preload loss. We focus here on a case of study in which a non-conventional release mechanism is tested for a mission-critical operation.

In the frame of space missions, many instruments are developed exploiting an extended free-falling object inside a reference sensor [5]. Scientific missions for geodesy and Earth observation employ free-falling objects as sensing bodies, sometimes exploiting them as a reference for the spacecraft attitude and orbit control system (AOCS). The instrument provides a reference signal produced by unwanted external forces (e.g. drag) to be compensated for by the thrusters [6,7]. Among these missions, we can cite Champ [8], Grace and Grace follow-on [9], Goce [10] and Swarm [11]. For fundamental physics missions, these instruments are used to test relativity. Among these missions, we can cite Gravity Probe B [12], Microscope [13], TianQin and Taiji [14], and LISA Pathfinder (LPF, [15]). LISA Pathfinder is an ESA technology demonstration mission for the in-flight testing of key technologies for the detection of gravitational waves from space [16]. Its primary science goal is to set into a pure geodesic trajectory a 2 kg gold coated AuPt cubic test mass (TM), reducing any force noise below $10\,\mathrm{fN}/\sqrt{\mathrm{Hz}}$ in the measurement bandwidth (1–30 mHz). The gravitational reference sensor (GRS, [17]), which hosts the TM, provides its position and attitude signals. The GRS can apply small forces (on the order of μN) and torques (on the order of pN m) by means of a set of gold-coated electrodes surrounding the TM. Large gaps (on the order of millimeters) are present between the TM and the electrode housing and any surface facing the TM is gold coated in order to limit the effect of uncontrolled electric fields (i.e., charge patches) on the purity of the free-fall trajectory. Given the heavy TM and the clearance between the TM and the electrodes, an additional challenge is the development of a launch-lock mechanism capable of protecting the hardware from the launch loads. This challenge posed also the need to take care of the detachment of the TM from the last mechanical interface in contact with the mechanism, and its injection into the geodesic trajectory. These challenges are addressed by means of two dedicated mechanisms, named Caging and Vent Mechanism (CVM) and Grabbing Positioning and Release Mechanism (GPRM). The CVM and the GPRM are aligned along the z axis of the TM reference frame, as schematically shown in Fig. 1.

The CVM [18] is a single-shot mechanism designed to secure the TM during the launch-phase. The CVM locks the TM through eight fingers, engaging its corners with a 10^3 N-order load (see Fig. 2(a)). The TM-CVM contact surfaces are challenged to provide the constraining force without local damage and relative slip between the two bodies.

The GPRM handles the TM in-orbit and is in charge of injecting it into the geodesic trajectory [19]. The GPRM is composed of two similar units, located on two opposite sides of the TM. Each unit, which is shown in Fig. 2(b), drives a cylindrical plunger. The plunger is designed to grab the TM by fitting into two pyramidal indents machined on two opposite TM faces. The indents are designed to provide guiding for the positioning of the TM without wear and stiction between the parts in relative motion. The two plunger heads have different shapes to avoid overconstraining the TM rotation about the z-axis. The plunger on the Z^- side of the TM has a pyramidal head, while the Z^+ side has a conical head.

The plunger is commanded along the z direction by a linear runner, which is actuated by a piezo-walk actuator. The linear runner is connected to the GPRM chassis via a slider-roller linear guide. A force sensor, connecting the plunger to the linear runner, measures the axial force applied by the mechanism to the TM. Inside each plunger, there is a coaxial gold tip actuated by a voltage-controlled piezo-stack actuator. When full voltage is applied to the piezo-stack, the tip is extended toward the TM until touching it on a dedicated surface. Conversely, when the commanding voltage is shorted, the tip retracts quickly. A redundant piezo-stack actuator is located inside the plunger in series to the nominal one, separated by a spacer mass. Nominal and redundant piezo are not operated simultaneously. The functionalities of the CVM and GPRM are summarized in Table 1.

Although AuPt contacts are not prone to cold welding [21], gold coating of the TM is necessary to provide highly conductive, homogeneous surfaces [17]. This ensures uniform TM potential, mitigating charge accumulation from cosmic rays, solar particles, and patch potentials, reducing the overall TM acceleration noise. However, adhesion forces at TM–GPRM mating surfaces cannot be reduced below the electrostatic actuation authority [22]. Consequently, a dynamic strategy is required for TM injection into the geodesic trajectory. The TM injection, which is also called TM release, relies on the quick and synchronous retraction of the two tips. The TM release is performed in three steps:

1. Pass-over, which is performed when the science phase must be initialized. The plungers are actuated toward the TM through the linear runner, engaging the indents on the TM (see Fig. 3(a)). The plungers motion is commanded until the preload exerted by their heads equals approximately 1 N. Once this condition is met, the CVM fingers are retracted, leaving the TM supported solely by the two plungers.
2. Handover, which is performed before the release, in order to relocate the TM constraining function from the plungers to the tips. The tips are moved toward the TM touching a dedicated surface, until a contact is established. The further extension of the tips is compensated by the retraction of the plungers, as shown in Fig. 3(b). At full extension of the tips, the contact load reaches about 300 mN and the TM is in pre-release configuration. At this point, the nominal distance between the plunger head and the TM indent is 14 μm

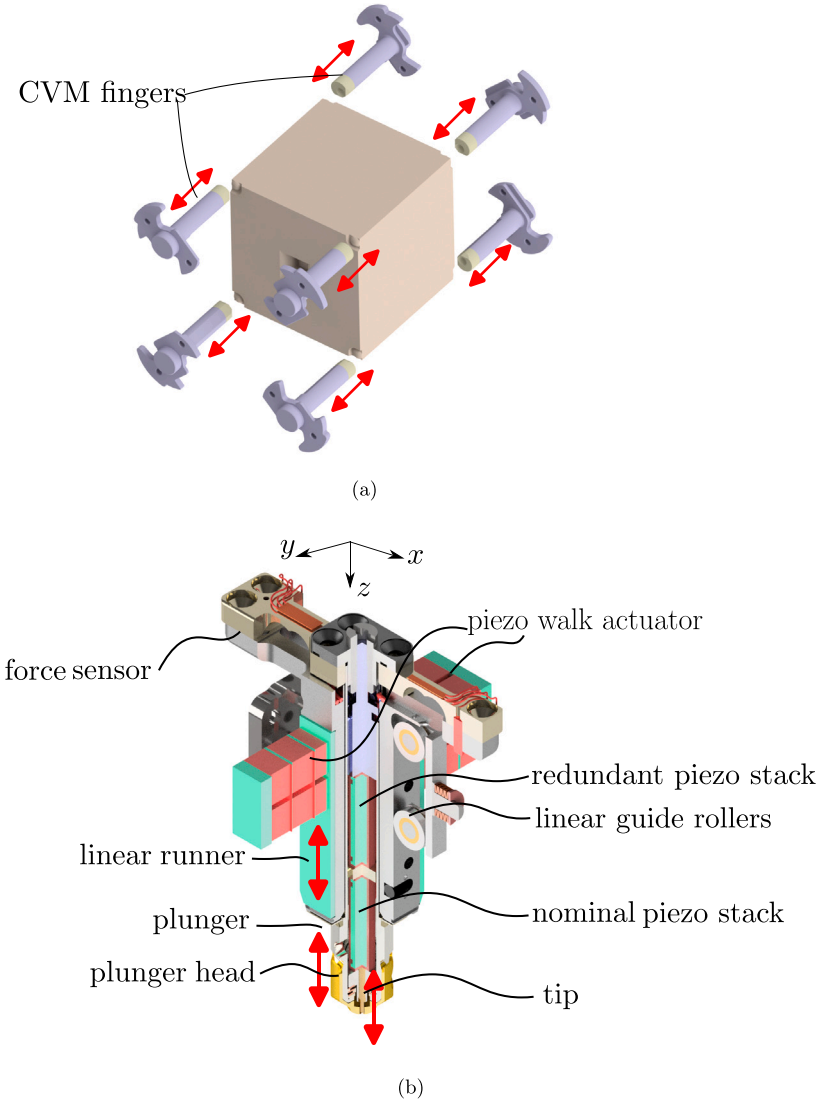

Fig. 2. On the left, exploded view of the CVM and its fingers. On the right, 3D section view of the GPRM. The red arrows indicate the moving parts. *Source:* Credits: [20].

Table 1
Mechanisms involved in caging and releasing the TM.

Mechanism	Function	Mechanism-TM interface
CVM	Caging the TM	Eight cylindrical fingers and TM vertices properly machined
GPRM	Grabbing the TM	Two plungers heads and dedicated TM pyramidal indents
GPRM tips	Releasing the TM	Two gold tips and two surfaces machined on the TM

3. TM release, which is performed by quickly retracting the two tips (in less than 100 µs), as shown in Fig. 3(c).

Once the TM is released, the electrostatic actuation system controls it and guides the TM to its geodesic trajectory if its residual velocity remains below $\pm 5\,\mu m\,s^{-1}$. The requirements on the TM state after the release are reported in Table 2. These requirements are driven by the maximum electrostatic control force that the electrodes may provide. The symmetrical GPRM design and release procedure should ensure that the expected TM state only involves the z axis. Along this axis, the velocity requirement may be converted into a maximum momentum equal to $10\,kg\,\mu m\,s$.

The dynamic strategy adopted for the injection of the TM into the geodesic trajectory benefits of two aspects. First, the adhesive bonds arising at the opposed contacts develop two impulses that may partially balance each other, limiting the final release velocity. Second, in the unavoidable presence of adhesion asymmetry, the quick retraction of the tips reduces both impulses by limiting the time duration of the adhesive pull.

Table 2
Requirement on the TM state after release for the LPF TM.

	Value	Unit
Translations	0±200	µm
Rotations	0±2000	µrad
Linear velocities	0±5	$\mu m\,s^{-1}$
Angular velocities	0±100	$\mu rad\,s^{-1}$

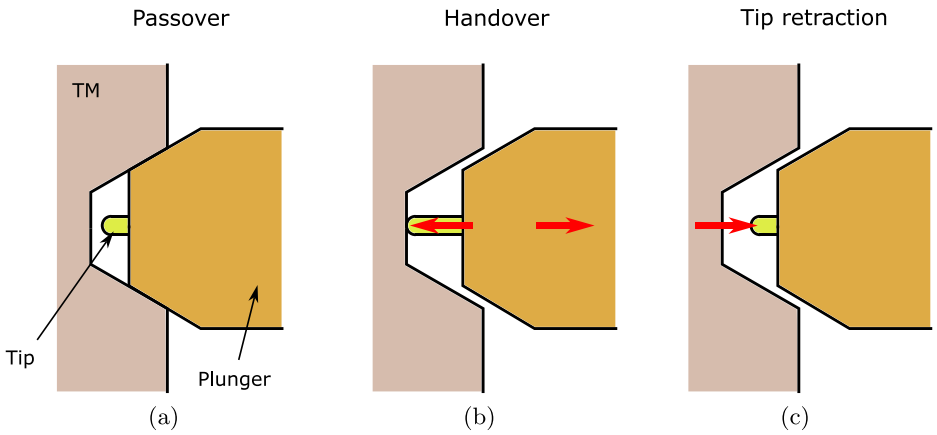

Fig. 3. Steps performed to release the TM intro free-fall.

The initial operation of the release mechanism on board LPF produced anomalous TM states, characterized by unexpected TM release velocity components [23]. The in-flight test campaign performed at the end of the extended mission phase, together with on-ground tests performed on a mechanism Engineering Qualifying Model (EQM), provided useful information to understand the deviation of the mechanism performance.

In this paper, we focus on the comprehensive testing activity, performed both on-ground and in-flight, related to the release mechanism and its release function. The combined ground-based and in-flight test strategy of the injection into geodesic function is presented. The paper is organized as follows. In Section 2 the TM injection into geodesic trajectory conceptualization and qualification is presented along with the actual in-flight TM release dynamics. In Section 3 the on-ground testing performed to investigate the in-flight anomalies is discussed and a model to explain those anomalies is developed. In Section 4 the compatibility between the in-flight and on-ground data is analyzed. In Section 5 the main conclusion are drawn and further developments are discussed.

2. The injection into geodesic trajectory: from on-ground conceptual testing to hardware qualification

The need for an experiment to conceptually test the injection phase is identified early in the mission definition phase. In the absence of a design of a release-dedicated mechanism, the test initially addresses the estimation of the level of impulses produced by the separation of gold-coated adhering surfaces in representative conditions (vacuum, cleanliness, surface material and roughness) of the in-flight environment. The Transferred Momentum Measurement Facility (TMMF, [24,25]) is designed to suspend a lightened mock-up of the TM as a simple pendulum inside a vacuum chamber. A laser interferometer is employed to measure the oscillation of the test mass produced by the separation from a body initially set into contact and then retracted. The transferred momentum is obtained by analyzing the oscillation signal through different techniques. The proposed test configuration benefits of two properties. First, the sensitivity of the experiment is enhanced by the adoption of a light test mass. Second, a one-sided release is studied, avoiding the cancellation of the opposite impulses present on the in-flight release mechanism.

The *conceptual* test is performed by suspending also the release tip as a simple pendulum (same length of the TM mock-up pendulum), as shown in Fig. 4. The tip is actuated through a thin wire. This setup allows to apply a limited contact force (μN), to limit shear forces at the contact patch and to minimize the effect of micro-seismic vibration [26]. This experiment characterizes the bottom limit of the impulse at release, produced by an *ideal* mechanism able to handle the test mass

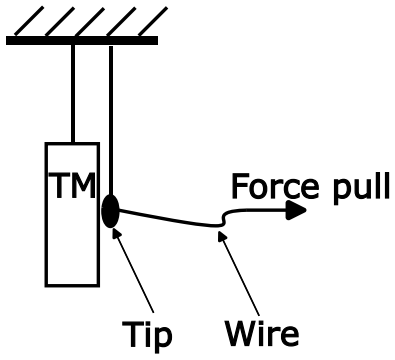

Fig. 4. Schematic illustration of the first development of the TMMF. The tip is suspended as a pendulum and is actuated through a thin wire.

with a very low contact force. The experiment design target is to minimize any spurious action on the adhesive bonds, potentially leading to under-estimation of the transferred momentum. The design must also maximize the measurement resolution to accurately capture the true dynamics of the event. A facility development plan is implemented testing different actuation systems of the adhered body and analyzing the resulting transferred momentum [27]. In this configuration, the analysis is limited to the pendulum swing motion, and the system is modeled as an oscillator with a single degree of freedom. The maximum measurement resolution is reached thanks to the application of optimal filtering techniques (Wiener–Kolmogorov) to the test mass mock-up displacement signal to estimate the impulse and the initial position of the suspended mass. The measured transferred momentum spans the range from 10^{-9} to $10^{-7}\,\mathrm{kg\,\mu m\,s^{-1}}$ [26,28].

The setup is upgraded in order to apply a controlled preload to the tip-TM contact. An adjustable blocking system is introduced to balance the preload force, engaging the TM mock-up on the opposite side with respect to the retracted body. The blocking mechanism consists of three needles coated with an anti-adhesive layer. This solution is used to balance the preload between a mock-up of the TM and the mock-up of the release tip, which is pushed against the former by a commanded fork (see Fig. 5). This setup allows to apply contact forces up to 100 mN, which are relaxed to a negligible level (i.e. μN) before the tip retraction. The system dynamics is modeled considering both the pendulum swing motion and the actuator displacement. The dynamical model is fitted to the measured signals of the mock-up and actuator motions, providing a measurement of the transferred momentum [29]. The estimated transferred momentum spans the range from 10^{-2} to $1\,\mathrm{kg\,\mu m\,s^{-1}}$, according to the commanded acceleration of retraction of the adhered body. This result confirms that the injection into geodesic

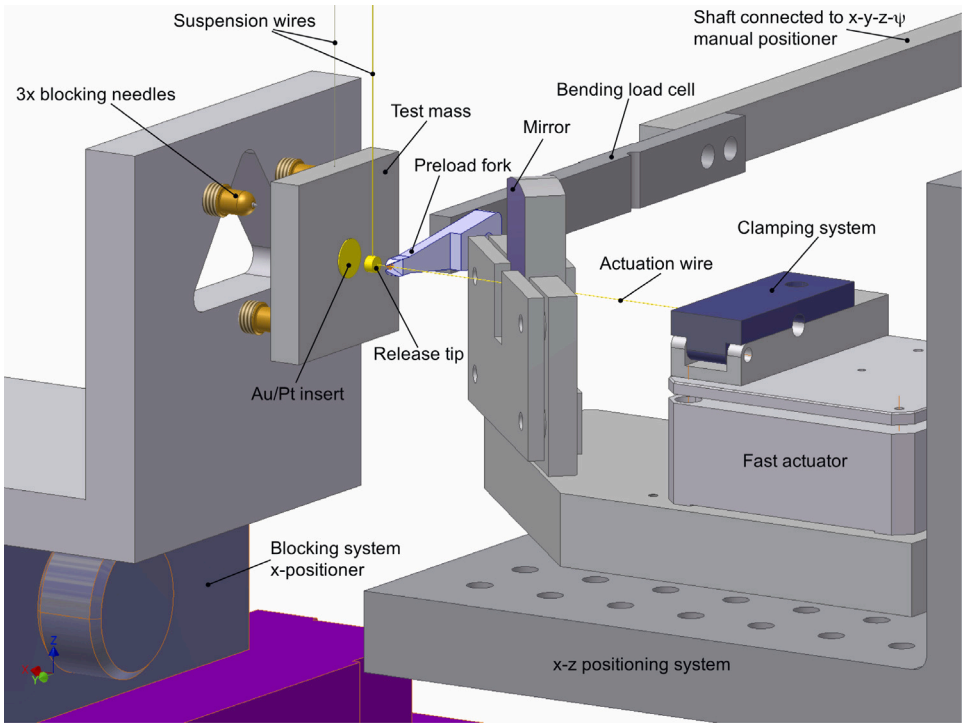

Fig. 5. Second development of the TMMF. Solid model of the double pendulum configuration. The tip is actuated through a thin wire. The preload fork allows to reach contact forces up to 100 mN.
Source: Credits: [31].

in the GRS system from a mechanism is possible. At least one order of magnitude of margin exists between the momentum transferred to the TM by an *ideal* mechanism and the control authority of the electrostatic actuation.

Analyses on the release tip surface demonstrate the formation of local welds and subsequent ductile rupture at the separation of the adhered body. The relationship between adhesion force and elongation is obtained indirectly [30], providing the experimental evidence of the dependence of adhesion forces on the separation distance between the contacting bodies.

According to the development plan of the GPRM, the TMMF is upgraded to apply a larger contact force. The double-pendulum configuration is substituted with a solution in which a direct actuation of the mock-up of the release tip is performed (see Fig. 6). An ultrasonic piezo stage drives the tip, engaging the TM mock-up at the gold-coated insert. The actuator is mounted on top of a tip-tilt and a rotating stage. This allows both the possibility to increase the preload to 400 mN and to change the tip retraction direction. The physical properties of the contacting bodies (bulk AuPt alloy, machining and coating process) are updated according to the design status of the GPRM, in order to provide a more representative test setup. The momentum transferred to the TM mock-up is now estimated by analyzing its acceleration, after removing the systematic contribution of the blocking system [32]. The repeatability of the force-to-elongation relationship is increased and the estimated transferred momentum increases further, up to 70% of the requirement [32]. Such a criticality highlights the need to proceed with a proper investigation of the performance of the flight hardware. This investigation provides a qualification of the final mechanism design for the specific function of releasing the TM into free-fall for its injection into the geodesic.

The prediction of the in-flight behavior of the GPRM based on the ground tests aims at extrapolating the results to the actual mission performance. The prediction considers that the in-flight injection is performed by two mechanisms. The mechanisms are characterized by a faster actuation of the release tips compared to the ground-tested mock-up. These conditions are expected to reduce the criticality of the TM release with respect to the test configuration. The results extrapolation to flight conditions is performed using a mathematical model of the injection dynamics, ensuring consistency between experimental data and the actual in-flight injection. The model combines the electromechanical dynamics of the GPRM [33,34] with the adhesion force model [35]. The mathematical model is employed to simulate different in-flight release scenarios, estimating the margin of the actual injection with respect to the requirement. The results extrapolation to flight conditions demonstrated that the requirements set on the TM release velocity should be fulfilled in at least 96% of the releases [36]. Moreover, the expected release velocity produced by adhesion is compliant with the requirement to within a factor 5 [32].

The qualification of the final design is performed by the integration of a GPRM engineering qualifying model (EQM) in the TMMF (see Fig. 7). The release tip shape and material, the preloading system and the retraction actuation are fully representative of the in-flight conditions. In parallel, the on-ground testing activities of the GPRM show that no significant contact load relaxation may be performed before the release phase, which must be realized with a residual preload force nearly equal to the maximum [37]. This boundary condition strongly affects the mechanics of the contact, the adhesion strength and, in turn, the transferred momentum. Moreover, the presence of a large preload at the retraction of the release tip introduces a dominant systematic error in the measured release velocity, produced by the elastic push of the blocking needles on the test mass mock-up when the preload is recovered.

The increased speed of the piezo-stack actuator compared to the previous configuration (based on an ultrasonic piezo actuator) reduces the duration of the adhesive force by an order of magnitude [38]. Dedicated ground-based testing campaigns show that the elastic push persists for several tenths of a ms, whereas the adhesive force exerted by the tip fades to zero to within tens of μs [36]. Therefore, a proper data analysis and result synthesis technique need to be adopted to extract the required information from the test results. The technique, which is presented in [39–41], leverages an observable of the released body

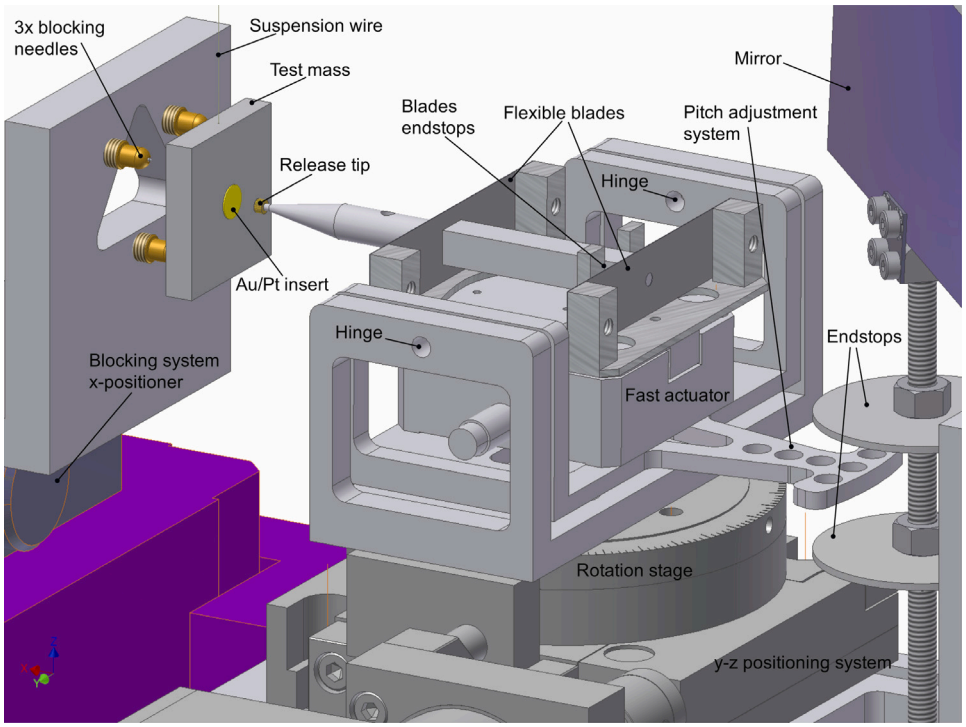

Fig. 6. Third development of the TMMF. Solid model of the mock-up of the release mechanism.
Source: Credits: [31].

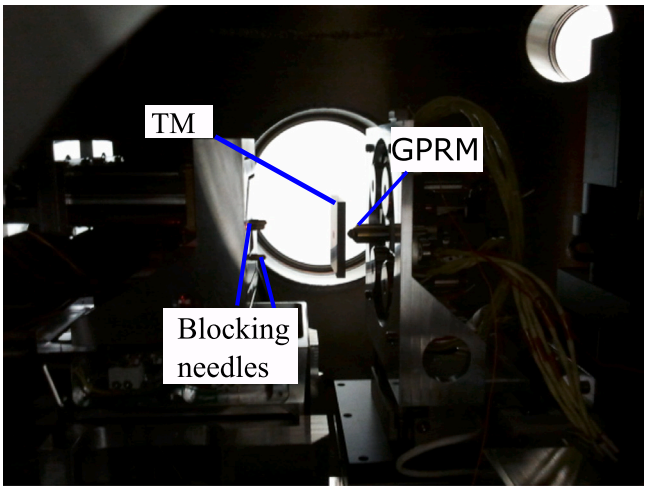

Fig. 7. Final TMMF configuration. The GPRM EQM is integrated in the TMMF.

dynamic response, i.e. its excited modes of vibration. The technique allows to refine the prediction of the adhesion contribution to the transferred momentum. The results show that, in the worst-case scenario, the contribution of the adhesion impulse to the overall transferred momentum covers 15% of the available momentum budget (i.e. up to $1.5\,\mathrm{kg\,\mu m\,s^{-1}}$).

2.1. In-flight testing of the injection phase

The LPF mission telemetry data show that, for the majority of the in-flight releases, out-of-requirement TM velocity components are common along all linear and rotational axes [42,43]. Moreover, the predominant component of the velocities is not the z component, meaning that the actual in-flight dynamics is different from the expected one-dimensional TM release.

As discussed in [44], the unexpected velocities are explained with collisions between the TM and the GPRM plungers at the tip retraction. These collisions occur if the gap between the plunger heads and the TM indent surfaces is not sufficient to compensate some clearance reduction effects occurring at the tip retraction (see Fig. 3(b)). The reduction of the clearance may be caused by several factors. Among these, studies have identified excessive plunger vibrations generated by the tip retraction [45], misalignment of the TM-plunger relative pre-release position [46], and non-rectilinear motion of the plungers during the release procedure [47].

In order to increase the available data on the in-flight performance of the GPRM, a dedicated in-flight test campaign of 96 TM releases is performed at the end of the extended mission phase. The preload exerted by the tip was modified from its nominal value of 300 mN, exploring its influence on the release dynamics of the TM.

The estimation of the TM release velocities in these tests is non-trivial, mainly because the telemetry sampling frequency is low (10 Hz). The low sampling frequency prevents the detection of collisions and hinders the separation of effects arising from time lags in the retraction of the two tips. In some tests, the reliable estimation of the velocity is not feasible, as the telemetry signals are noisy and hardly interpretable. In other cases, the TM results prematurely released during the handover procedure showing non-zero velocity components before the retraction of the tips. Consequently, a test is considered reliable only if it results free from all these phenomena [44]. If we analyze the TM momentum at the release in the tests whose velocities can be reliably estimated (45 total tests), it is possible to disentangle the effects of the spurious plunger-TM interaction along the different axes. The disentanglement allows to extract the underlying nominal dynamics taking place along the z-axis.

The model developed for this calculation is based on the linear system of the Newton-Euler equations of the TM dynamics. The dynamics is written in the impulsive form, expressing the effect of the TM-plunger interaction in terms of their time integral. The overall impulse developed after the tip retraction is associated to the variation of the TM momentum. In the model, the geometry of the TM indents is taken

Table 3
TM mechanical and geometrical parameters. The values are estimated from the CAD model of the TM and the plunger heads.

Param.	Value	Unit	Description
a	21.8	mm	Distance of the predicted TM-plunger contact point from the plane x–y estimated using the CAD model of the GPRM
b	3.9	mm	Distance of the predicted TM-plunger contact point from the planes x–z or y–z estimated using the CAD model of the GPRM
α	41.5	°	Inclination of the TM indent contact surfaces with respect to the z axis
J_{jj}	678×10^{-6}	kg m^2	TM inertia about $j \in \{x, y\}$ axis
M	1.98	kg	TM mass

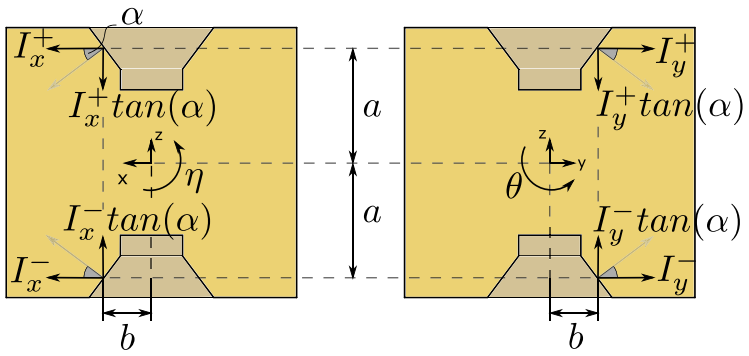

Fig. 8. Cut views of the TM together with the impulses produced by the plunger-TM interaction.

into account and the orthogonality of the impulses to their surface is imposed [23]. In Fig. 8, two cut views of the TM are depicted together with the impulses produced by the plunger-TM interactions. The model, defined by the system of Eqs. (1), relates the lateral impulses (x and y directions) with the TM momentum along z. The inputs to the model are the mechanical and geometrical characteristics of the TM (see Table 3) and the velocities recorded in-flight; the outputs are the impulse received by the TM at the release along x, y and z.

$$\begin{cases} +I_x^+ + I_x^- & = M v_x \\ +I_y^+ + I_y^- & = M v_y \\ (-I_y^+ + I_y^-)(a + b\tan\alpha) & = J_{xx}\omega_\theta \\ (+I_x^+ - I_x^-)(a + b\tan\alpha) & = J_{yy}\omega_\eta \\ (|I_x^-| + |I_y^-| - |I_x^+| - |I_y^+|)\tan\alpha + I_{z,res} & = M v_z \end{cases} \quad (1)$$

where I_j^i represents the impulse along the jth direction (x, y or z) received by the TM from the ith plunger (+ or −, representing the conical and pyramidal plunger respectively). Moreover, v_i and ω_j represent the in-flight TM linear ($i = \in \{x, y, z\}$) and angular ($j = \in \{\theta, \eta\}$) velocities components respectively.

The model allows the estimation of the residual impulse along z, called $I_{z,res}$, which contains all the effects along the z direction that are not explained by the projection of the lateral impulse caused by the plungers' impact.

The model is applied to all the 45 in-flight reliable tests, providing a value of the TM residual momentum for each one. These values are divided in three groups, based on the in-flight residual preload: group one collects the estimated $I_{z,res}$ values for the tests with a preload ranging from 50 to 200 mN (9 values), group two collects the values for the tests with a preload ranging from 200 to 400 mN (4 values) and group three collects the values for the tests with a preload ranging from 400 to 600 mN (6 values). Tests with preload lower than 50 mN are discarded since their uncertainty make them compatible with zero contact force, i.e. unstable contact. This choice is further supported by telemetry data, which highlight that in some tests at 50 mN, the tip is not in contact with the TM prior to its release. For each group, the mean values of the preload and of $I_{z,res}$ are computed along with their standard deviation. The three $I_{z,res}$ mean values are referred to as $I_{z,res,100}$, $I_{z,res,300}$, $I_{z,res,500}$ since the mean preloads are equal to 129 mN, 292 mN and 521 mN respectively and are plotted in Fig. 17. In Section 4 they constitute the reference for the comparison with the on-ground results.

3. A combined ground–flight test analysis

In this Section, the analysis and following interpretation of the in-flight performance is proposed, focusing on its compatibility with the ground-based tests. The compatibility of the GPRM in-flight release performance with the requirements is investigated in the hypothesis that the spurious impacts are avoided. This option would support a possible mechanism partial re-design finalized at producing, in LISA, just the nominal release dynamics.

3.1. In-flight release dynamics

The in-flight release dynamics of the TM in the nominal configuration of the mechanism takes place along the common axis of retraction of the two tips. The equation of motion of the TM may be projected on that axis, which corresponds to the z direction in the GRS reference frame. Along z, the two contact forces between the TM and the release tips start from an equal and opposite compression. Then, at the retraction of the tips, the contact forces follow two different time histories, as shown in Fig. 9. The differences between the two time histories are described in principle by the following parameters:

- the time lag t_D, defined as the difference between the start time of the two tips;
- the different retraction velocities of the tips, producing different force drop times t_1^+ and t_1^- at the two contacts ($t_1^+ - t_1^- = \Delta t_1$);
- the different adhesive pull at the two contacts, defined as $\Delta\imath$.

By equating the momentum acquired by the TM to the net impulse of the two forces, the three effects combine as shown in Eq. (2).

$$I_{z,res} = f_0\, t_D + \frac{1}{2} f_0\, \Delta t_1 + \Delta\imath \quad (2)$$

where $I_{z,res}$ is the in-flight TM residual momentum along z (see Section 2.1), f_0 is the preload on the TM, measured in-flight, just prior

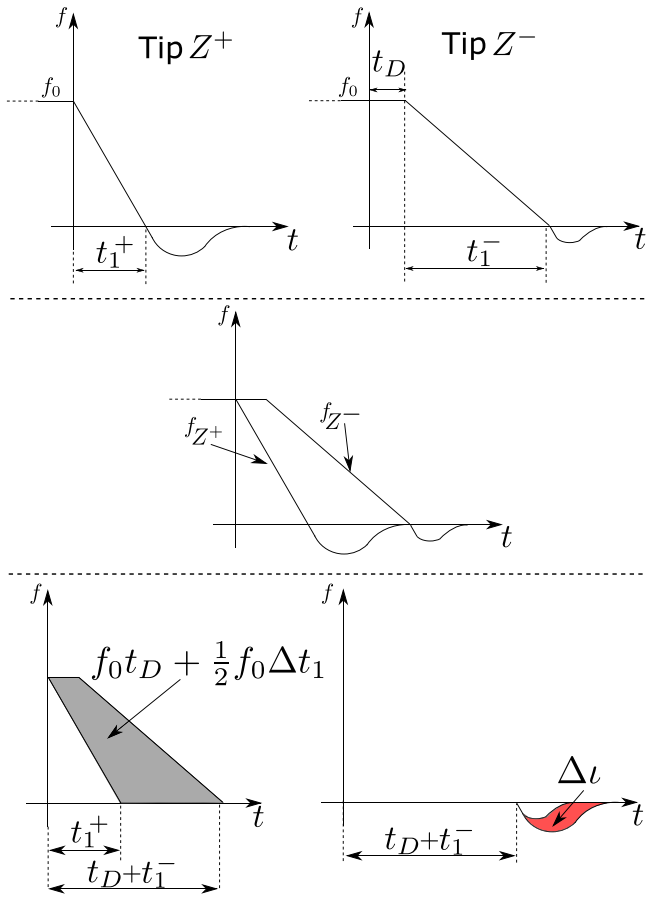

Fig. 9. Schematic contact force time histories on the opposite TM sides.

to the tip retraction. Eq. (2) shows that a net TM momentum arises at release as a consequence of the asymmetry of the two mechanisms and is affected by the repeatability of the asymmetries described above. The equation expresses the momentum budget for the TM combining the three contributions produced by the time lag, the velocity of retraction and the adhesive pull respectively.

The left-hand side of the momentum budget of Eq. (2) expresses the residual (i.e. impact-free) in-flight momentum along the z-axis. The right-hand side of the same equation provides its estimation based on the ground tests. Those terms are assumed to be random quantities, whose sum must comply with the release velocity requirement. Noteworthy, the terms depend on the dynamic response of the TM to the applied force time history and would require the solution of its equation of motion. For example, Δt_1 depends on the motion of the tip with respect to the TM. However, because the velocity of the tip is four orders of magnitude larger (on the order of $10^4\,\mu m\,s^{-1}$ against $1\,\mu m\,s^{-1}$), the effect of the TM response is negligible. The aforementioned contributions are analyzed in the following.

3.2. Contribution of the tips retraction time lag

The first contribution of Eq. (2), $f_0 t_D$, combines the preload at the release and the time lag between the retraction of the two tips. To measure the time lag between the mechanisms a dedicated experimental setup is built, as shown in Fig. 10.

Two units of the GPRM EQM mechanisms (conical and pyramidal) are mounted on an anti-vibration platform with the plungers mutually aligned. A gold insert, machined to reproduce the TM landing area, is mounted on a friction-less pendulum and aligned with the plungers. The pendulum suspension guarantees that, along the common axis of retraction of the tips, the test mass mock-up is in nearly free-fall state.

The plungers are electrically connected to the cathode of a battery and the gold insert is connected to the battery anode. In this way, whenever a mechanism is in contact with the insert, the half-circuit related to that plunger is closed and a current flows.

To perform the measurement, the release tips are extended and set in contact with the gold insert by using the plungers actuators, until a desired preload is reached. Since the tip is in electrical contact with the hosting plunger, when the tips are touching the gold insert a voltage difference is present on the ends of two high-precision $10^1\,k\Omega$ resistors R (see scheme of Fig. 10). Their resistance is chosen to limit the current and to guarantee a circuit characteristic time constant on the order of μs (i.e., lower that the expected time lag). The release tips are finally retracted, causing the voltage to drop to zero as soon as the electrical contact between a tip and the insert is opened. The voltage drop signals across each resistor are measured by two channels of a DSO7032A Agilent Technologies digital oscilloscope. Each measured voltage signal is then fitted with a piecewise function:

$$\begin{cases} V_0 & t \le t_0 \\ V_0\, e^{-\frac{t-t_0}{CR}} & t_0 \le t \end{cases} \tag{3}$$

where V_0 represents the battery voltage, t_0 is the time instant corresponding to the detachment of the tip from the insert and C is the circuit capacitance (measured on the order of 10^{-10} F). In Fig. 11 the two measured voltage signals (blue curves) of a test are plotted together with their fitting function (red curve for the pyramidal plunger, orange curve for the conical one), as an example.

For a given test, the difference between the two fitted values of t_0 gives an estimation of the time lag between the retraction of the tips. The experiment is repeated for a total of 70 times, varying the preload from 100 to 500 mN, providing an experimental mean value of the time lag equal to $11 \pm 4\,\mu s$ (1σ error interval). It is worth noting that the sign of the time lag does not depend on the applied preload and is essentially systematic, that is one of the tip is almost always retracting before the other.

The statistical distribution of the preload f_0 is based on the dispersion of the measured GPRM preload force during in-flight testing before every release. Assuming that f_0 and t_D are independent random variables with probability density functions $h_1(f_0)$ and $h_2(t_D)$ respectively, the probability density function of their product is calculated as the Mellin convolution of $h_1(f_0)$ and $h_2(t_D)$:

$$PDF_{f_0 t_D}(z_1) = \int_{-\infty}^{\infty} h_2(z_2)\, h_1\left(\frac{z_1}{z_2}\right) \frac{1}{z_2}\, dz_2 \tag{4}$$

where z_1 and z_2 correspond to f_0 and t_D respectively.

As an example, the result of the calculation is plotted in Fig. 12 where $h_1(f_0)$ describes the probability density function of the in-flight preload corresponding to the 300 mN tests group.

Fig. 12 shows that in the nominal case in approximately 99% of the cases the time lag contribution falls between $0\,kg\,\mu m\,s^{-1}$ and $7\,kg\,\mu m\,s^{-1}$. Furthermore, in approximately 13% of the cases the momentum contribution falls in the range $5–8\,kg\,\mu m\,s^{-1}$, eroding up to 80% of the maximum available momentum budget (i.e. $10\,kg\,\mu m\,s^{-1}$).

3.3. Contribution of tips-TM adhesion

The adhesion contribution is characterized by means of a dedicated ground testing campaign. The tests are performed with the TMMF, where a one-sided release is realized with the EQM of the GPRM. A picture of the TMMF is shown in Fig. 7. The design of the TMMF guarantees the reproduction of the in-flight environmental conditions:

- the experiment is performed in a vacuum chamber; by means of a ion pump the pressure is constantly kept at a 10^{-7} mbar level and the cleanliness level is guaranteed;

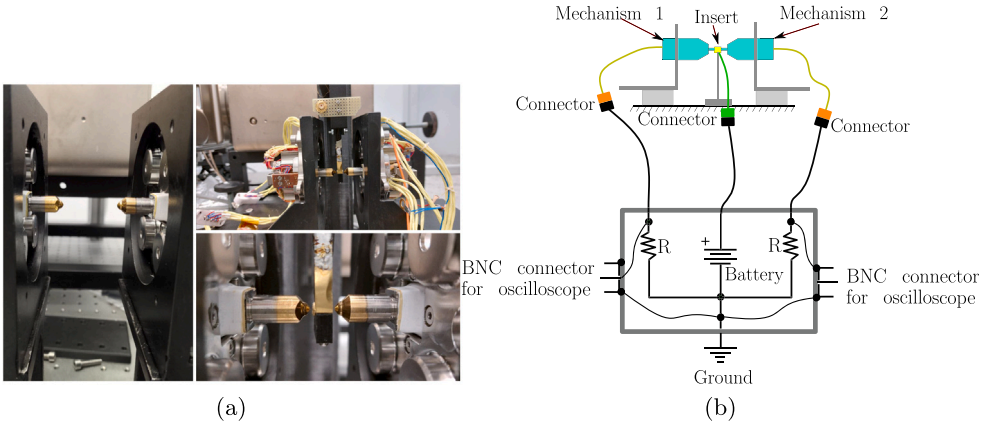

Fig. 10. Left: experimental setup for the measurement of the time lag between the retraction of the two tips. Right: schematic electrical scheme of the experimental setup.

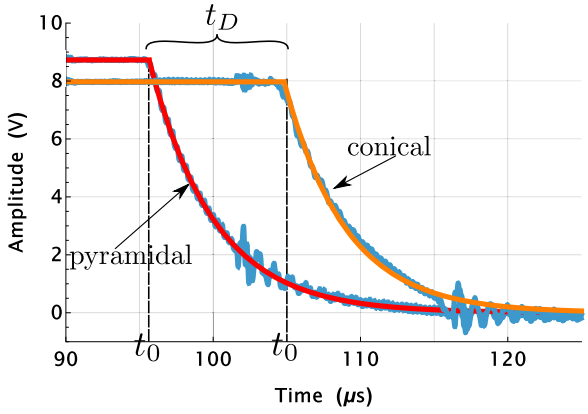

Fig. 11. Zoomed plot of the experimental voltage drop for the two plungers (in blue curves). The discharge time history (red and orange curves) is fitted to the corresponding signal, providing an estimation of the instant t_0. The difference between the two time instants provides the time lag t_D between the two fitting curves.

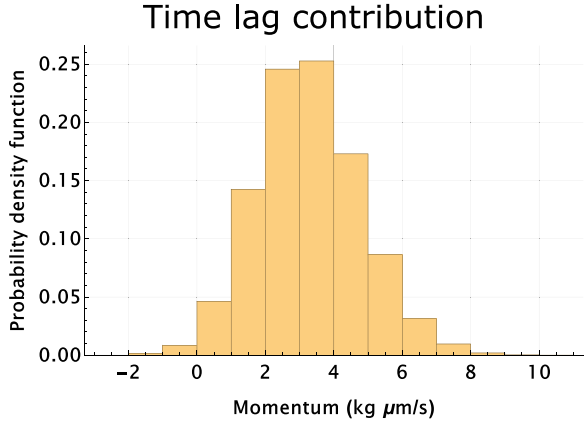

Fig. 12. Distribution of the time lag contribution $f_0 t_D$ to the momentum budget computed with the ground and in-flight test data (300 mN preload group).

- the vacuum chamber is assembled over an active anti-vibration platform in order to isolate the system from micro-seismic noise;
- the devices are electrically grounded in order to minimize disturbing electrostatic forces at their contact;
- the free-fall state is simulated through a pendulum wire that hangs the test mass mock-up. The pendulum wire also contributes to minimize vibrations transferred by the chamber to the test mass mock-up;
- the system temperature, representative of the in-flight conditions, is controlled.

The measurement system is composed of a SIOS SP-S 120 laser interferometer (which provides the displacement of the test mass mock-up), an optical lever (used in the preliminary alignment operations and as diagnostic signal), and a high-speed camera (which allows to constantly monitor the relative position of the devices during the operations). The GPRM EQM, the blocking system and the TM mock-up, constitute the core of the experiment (Fig. 13). The blocking system is composed of three horizontal needles. The stiffness of the needles is comparable to the axial stiffness of the GPRM. The needles are coated with a conductive anti-adhesive layer CrN-based and are designed to minimize adhesion at the needle–TM interface. The TM mock-up is the sensing body to which a single one-sided adhesive impulse is applied. It consists of a 36 × 36 × 4 mm^3 W-alloy parallelepiped, hang through a pendulum wire to the top of the TMMF; in its center, a cylindric insert is press-fit by interference coupling. The insert is gold coated, to reproducing the in-flight landing area properties (i.e., the contact surface between in-flight TM and GPRM).

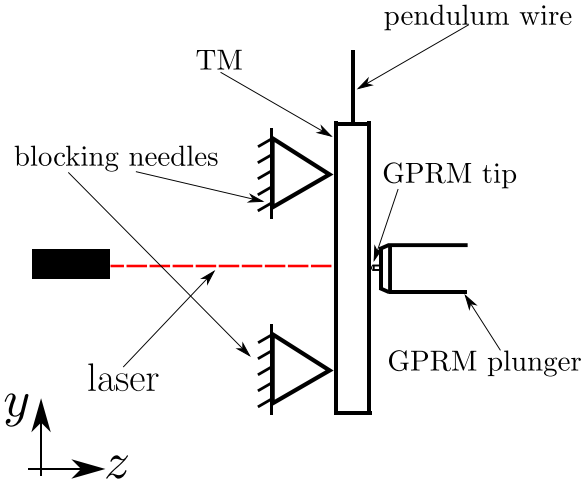

Fig. 13. Schematic sketch of the experimental setup. The red dotted line represents the laser beam.

The total mass of the mock-up (88.5 g) is approximately 20 times smaller than the in-flight one, yielding an equivalent amplification of the velocity produced by the adhesive impulse. The length of the wire (slightly more than 1 m) makes the natural period of the pendulum oscillator much larger than the duration of the release experiment. Therefore, it is possible to neglect the effect of gravity for typical displacements (about 1 μm) around the equilibrium position occurring during the tests.

The displacement of the mock-up along the horizontal release direction (corresponding to the z axis) is sampled at a 200 kHz frequency by means of the laser interferometer. The laser interferometer has a nominal wavelength of approximately 633 nm and is designed for the measurement of mechanical vibrations in the sub-μm range.

The test procedure is composed of the following steps:

- Alignment. The interferometer optical axis, the blocking system, the mock-up frame and the GPRM plunger are mutually aligned by means of linear and angular micrometric positioners. Firstly, the interferometer optical axis orientation is adjusted in order to reach the orthogonality with respect to the vertical direction. The position and orientation of the GPRM are adjusted through a tip-tilt stage while pointing the laser beam at the tip. The blocking needles attitude is adjusted by minimizing the variation of the test mass attitude during the blocking phase.
- Blocking. The blocking needles are commanded to approach the mock-up until an incipient contact is established, i.e. its yaw oscillation is negligible. When the mock-up is still, the plunger is actuated toward it, until the tip engages the mock-up with the target preload. The preload value is measured in real time by the GPRM force sensor. The adhesion produced by the contact between the needles and the TM is negligible, as demonstrated in [34].
- Release. When the release command is sent to the GPRM unit, the voltage signal sent to the release tip piezo-stack actuator drops and the tip is quickly retracted (approximately 10^4 μm s^{-1}). The tip applies to the mock-up a decreasing contact force, which converts into an adhesive pull contributing to the mock-up momentum. At the same time, the needles act as preloaded spring rigidly pushing the mock-up from the rear side. The elastic push produces an additional contribution to the overall momentum acquired by the mock-up. When the mock-up detaches from the needles, it moves with a constant velocity along z axis (free flight velocity), and the experiment is concluded.

The ground-based experiment reproduces a one-sided release with a rescaled dynamic, i.e., an enhanced sensitivity to the applied forces. The one-side experiment allows to neglect the effect of any time lag with respect to the release commanding signal on the release dynamics. However, a disadvantage of the one-sided release is that the needles push has a significant effect on the TM final velocity. Assuming that the system behaves as a preloaded oscillator, the velocity is amplified of a factor equal to the square root of the flight to mock-up mass ratio, i.e., about 4.

The output of the experiment (Fig. 14) is the z displacement of the mock-up, measured by the interferometer. The acquisition is triggered by the piezo-stack voltage drop. As shown in Fig. 14, the measured displacement can be divided into three main parts. The first part corresponds to the pre-release interval: the mock-up is still, blocked by the needles and the tip. In the second part, named acceleration interval, the momentum is transferred to the mock-up. A small fraction of the total momentum is transferred by the adhesive pull (duration approximately 20 μs, [39]) while the majority of the transferred momentum is due to the needles relaxation (duration approx 500 μs). In the third part, the mock-up detaches from the needles and moves with a constant velocity.

Different preload values are tested, repeating the experiment 140 times and collecting the results in three different subsets: 10 experiment

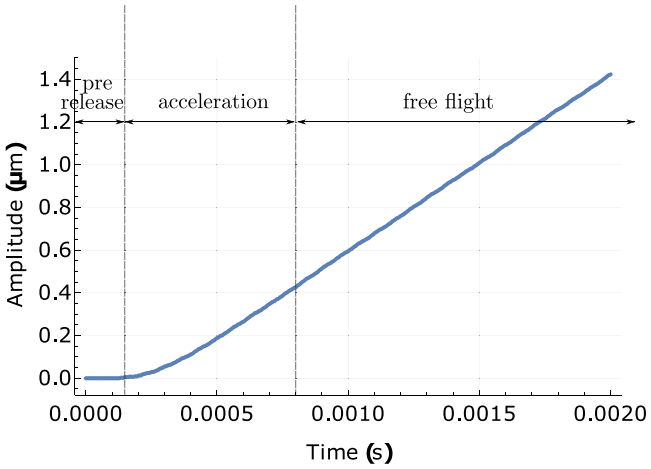

Fig. 14. Measure of the TM mock-up displacement during an adhesion test. The curve is divided in three intervals, according to the TM state: still, accelerated, constant velocity.

are performed applying 100 mN, 120 applying 300 mN (which is the in-flight nominal value of the preload) and 10 applying 500 mN.

A measurement technique is developed to disentangle the effect of the needles relaxation and the adhesive impulse in the overall momentum. The technique exploits the excited vibration modes of the TM mock-up and is briefly summarized below (a detailed description is provided in [39–41]. The TM mock-up is modeled as a deformable bidimensional plate. Its motion $z(t)$ may be written as the sum of the N excited vibration modes [48]:

$$z(t) = \sum_{m=1}^{N} \alpha_m(x, y) q_m(t) \tag{5}$$

where $\alpha_m(x, y)$ is the $m-$th mode shape evaluated at coordinate (x, y) in the mock-up body-fixed reference frame, and $q_m(t)$ represents the corresponding modal coordinate. Each modal coordinate is obtained by solving the equation of motion of a simple harmonic oscillator:

$$q_m''(t) + \omega_m^2 q_m(t) = \frac{Q_m(t)}{\beta_m} \tag{6}$$

where ω_m is the natural frequency of the $m-$th mode, β_m the corresponding modal mass and $Q_m(t)$ the modal projection of the forces acting on the mock-up. The modal projection is the sum of two contributions. The first contribution represents the projection of the adhesion force exerted by the tip, which is function of distance between the adhered bodies [30]. The second contribution represents the projection of the force exerted by the needles. Each needle is modeled as a preloaded spring connecting the mock-up to ground.

The solution to Eq. (6) yields the modal response of the $m-$th vibration mode. The squared amplitude of the steady-state response c_m is written as:

$$c_m^2 = \alpha_m^2(0, 0)\,(A_m^2 + B_m^2) = f(\imath, p, \omega_m, \beta_m, \alpha_m) \tag{7}$$

where $\alpha_m(0, 0)$ is the mode shape evaluated at the center of the mock-up (i.e., where the laser is pointing), A_m and B_m are the amplitudes of the sine and cosine components of the steady-state oscillations. These amplitudes are a function of the modal parameters, the preload p, and the intensity of the adhesion force impulse $\imath$.

Eq. (7) represents the adhesion impulse measurement technique. The left-hand side corresponds to the oscillation amplitude of the mth excited vibration mode. The amplitude of each mode is estimated applying an optimal filter to the acquired displacement signal [49]. The right-hand side represents the oscillations as a function of the modal parameters, the preload, and the adhesion force impulse. The parameter estimation procedure, applied to each of the three preload data subsets, is summarized in the following steps:

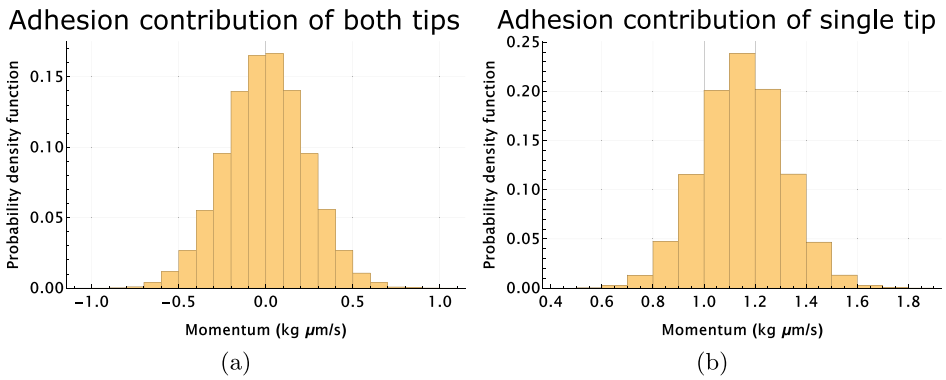

Fig. 15. Probability density function of the adhesion contribution to the TM release momentum. Left: adhesion on both tips. Right: worst case, adhesion on a single tip.

- a finite element model of the mock-up provides the values of the modal parameters
- an analytical model of the mock-up dynamics is fitted to the experimental signal. The fitting procedure allows the estimation of the preload force applied by the release tip (as an independent estimation with respect to the GPRM load cell measurement) and of the time range associated to the free-flight oscillations of the TM;
- the modal and fitting parameters are substituted in Eq. (7), which becomes function of just the adhesion impulse intensity $\imath$;
- computing the mean impulse intensity $\bar{\imath}$ and standard deviation $\bar{\sigma}_\imath$ over a given subset of measurements.

Assuming that the one-sided release tests are representative of the in-flight behavior, the statistic of $\Delta\imath$ (term appearing on the right hand side of Eq. (2)) corresponds to the difference between two random variables. The random variables are extracted independently from the same normal distribution centered in $\bar{\imath}$ and with standard deviation $\bar{\sigma}_\tau$. The probability density function of the sum of two random variables is calculated through the convolution of their respective PDFs:

$$PDF_{\Delta\imath}(z) = \int_{-\infty}^{\infty} PDF_\imath(-x)\, PDF_\imath(z-x)\, \mathrm{d}x \tag{8}$$

The PDF resulting from the calculation for the 300 mN data set is plotted in Fig. 15(a). The plot shows that in almost 98% of the cases this contribution falls between −0.5 and 0.5 kg μm s^{-1}.

Due to possible settlements of the TM during the handover phase, it cannot be excluded that the adhesive bonds produced at the tip-TM contacts are broken at one side before the release. This corresponds to a worst case in which only one tip is adhering to the TM landing area, reducing the mutual cancellation. In this case, the statistic of $\Delta\imath$ corresponds to the PDF of a single random variable, since the contribution of the other tip is equal to zero by hypothesis. The PDF resulting in this case is plotted in Fig. 15(b). Being this the worst case, the PDF shows that in at least 82% of the cases the momentum contribution falls in the range 1–1.5 kg μm s^{-1} covering no more than 15% of the maximum available momentum budget (i.e. 10 kg μm s^{-1}).

3.4. Contribution of the asymmetry of the tip retraction velocity

An estimation of the contact force drop time (t_1^+ and t_1^-) is found calculating the time required by the tip to travel the distance which recovers its elastic (Hertzian) penetration in the landing area (about 0.1 μm, [50]). From the aforementioned retraction tests performed on ground, it results that t_1 is 1.2 ± 0.4 μs. Assuming uncorrelated behavior of the two units of the GPRM, the difference between the duration of the unload ramps of the two contacts, Δt_1, has a standard deviation of 0.5 μs. Combining this reference Δt_1 with the average pre-load of 300 mN it results that this contribution is on the order of magnitude of 0.1 kg μm s^{-1}, i.e., it is negligible with respect to the other contributions. For this reason, the effect of different velocity of the release tips in the TM momentum, expressed by the term $f_0 \Delta t_1$ in Eq. (2), is hereinafter neglected.

4. Compatibility between in-flight and on-ground test results

As a consequence of the discussion of Section 3.4 Eq. (2) is approximated as shown in the following:

$$I_{z,res} \approx f_0 t_D + \Delta\imath \tag{9}$$

Given the probability density functions of $f_0 t_D$ and $\Delta\imath$ (see Sections 3.2 and 3.3), the PDF of the TM residual momentum $PDF_{\mathrm{TM}}(z)$ is found applying the rule expressed in Eqs. (4) and (8).

In Fig. 16 two PDF of the TM residual momentum are plotted together. The yellow histogram refers to the PDF of the TM residual momentum computed considering only one tip adhering to the TM, while the light blue one to the PDF computed considering both tips adhering to the TM. The Figure shows that the momentum prediction based on the on-ground tests is represented by a distribution in which the mean and the dispersion are dominated by the time lag contribution.

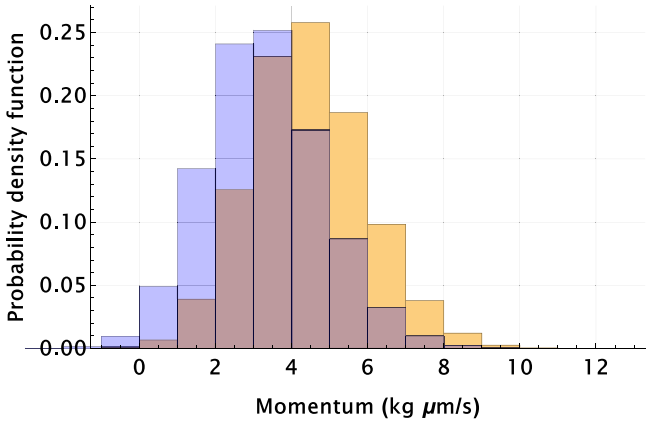

Fig. 16. Distribution of the overall TM residual momentum. Light blue: overall momentum considering adhesion on both tips. Yellow: overall momentum considering adhesion on a single tip.

As discussed previously, the on ground data-set are divided into three sets depending on the preload force. Three probability density functions are estimated from the ground tests: $PDF_{\mathrm{TM},100}$, $PDF_{\mathrm{TM},300}$ and $PDF_{\mathrm{TM},500}$, where the number in the subscript refers to the preload value in mN. Each of the three PDFs is compared with the distribution of the corresponding value of the flight data residual impulse, $I_{z,\mathrm{res}}$, indicated as $I_{z,\mathrm{res},i}$ (with $i \in \{100, 300, 500\}$). Such residual impulses

are found by grouping the in-flight data according to the preload force (as discussed in Section 2.1).

The statistical compatibility between the in-flight telemetry data and ground-based tests is checked with a test of hypothesis [51,52].

Let $\{x_{j,1} \dots x_{j,n_j}\}$ be the set of n_j values of $I_{z,res,j}$ belonging to the $j-$th group (with $j \in \{1,2,3\}$, see Section 2.1) and $\{y_{j,1} \dots y_{j,N_j}\}$ be a random sample of N_j observations from the corresponding $PDF_{\mathrm{TM,j}}$. Let $\bar{x}_j$, $\bar{y}_j$, $\sigma^2_{x,j}$ and $\sigma^2_{y,j}$ be the means and variances of the two samples and let $\mu_{x,j}$ and $\mu_{y,j}$ be the means of the two populations, respectively. We associate the null hypothesis H_0 to the case in which $\mu_{x,j} = \mu_{y,j}$ i.e. the in-flight $I_{z,res}$ and its ground-based pair are equal. When H_0 is true, the following statistics:

$$t^*_j = \frac{\bar{x}_j - \bar{y}_j}{\sqrt{\frac{\sigma^2_{x,j}}{n_j} + \frac{\sigma^2_{y,j}}{N_j}}} \tag{10}$$

is distributed as a t-distribution with ν_j degrees of freedom, where ν is equal to:

$$\nu_j = \frac{\left(\frac{\sigma^2_{x,j}}{n_j} + \frac{\sigma^2_{y,j}}{N_j}\right)^2}{\frac{\left(\frac{\sigma^2_{x,j}}{n_j}\right)^2}{n_j - 1} + \frac{\left(\frac{\sigma^2_{y,j}}{N_j}\right)^2}{N_j - 1}} \tag{11}$$

Chosen a significance level α, if the absolute value of the statistic t^*_j is lower than the corresponding two-sided t-student's distribution value $t_{1-\frac{\alpha}{2},\nu_j}$, there is no evidence of violation of H_0, which is not rejected.

The results of the comparisons are reported in Table 4, where α is set equal to 0.05 [51,52] and N_j equal to 50. In order to account for the limited number of components of the $I_{z,res}$ sets (due to the limited amount of in-flight tests), the comparison of the on-ground and in-flight TM momentum distributions is performed varying N_j from 10 to 100. The H_0 hypothesis is never rejected.

Table 4
Statistical compatibility of ground tests distributions and in-flight data with α equal to 0.05, N_1, N_2 and N_3 equal to 50.

Group	Degrees of freedom	$\lvert t^* \rvert$	$t_{1-\frac{\alpha}{2},\nu}$
100 mN	8	0.8	2.3
300 mN	3	0.5	3.2
500 mN	5	1.7	2.6

In order to include in the analysis all the possible cases that may have occurred in flight, the statistical compatibility of each group is carried out in two additional cases:

- case 1: only the Z^+ tip is adhered to the TM, i.e. the net impulse becomes $I_{z,res} \approx f_0 t_D + \iota$;
- case 2: only the Z^- tip is adhered to the TM, i.e. the net impulse becomes $I_{z,res} \approx f_0 t_D - \iota$.

The H_0 hypothesis is never rejected also for case 1 and case 2 (independently of N_j). The results of the statistical analysis carried out in the three cases are presented in Fig. 17, where three plots are depicted together. Fig. 17(a) shows the 9 values of $I_{z,res,100}$ (blue dots) and the three PDF corresponding to the three cases analyzed. Fig. 17(b) shows the 4 values of $I_{z,res,300}$ (blue dots) and the three PDF corresponding to the three cases analyzed. Fig. 17(c) shows the 6 values of $I_{z,res,500}$ (blue dots) and the three PDF corresponding to the three cases analyzed.

The statistical compatibility between the in-flight $I_{z,res}$ and their ground-based prediction constitutes a relevant confirmation of the effectiveness of the flight–ground testing activity. The compatibility indicates that the key factors influencing the nominal release dynamics are effectively identified. These findings provide strong support for the development of the GPRM for LISA, particularly in addressing the effects that caused unexpected performance. We summarize these findings in the following:

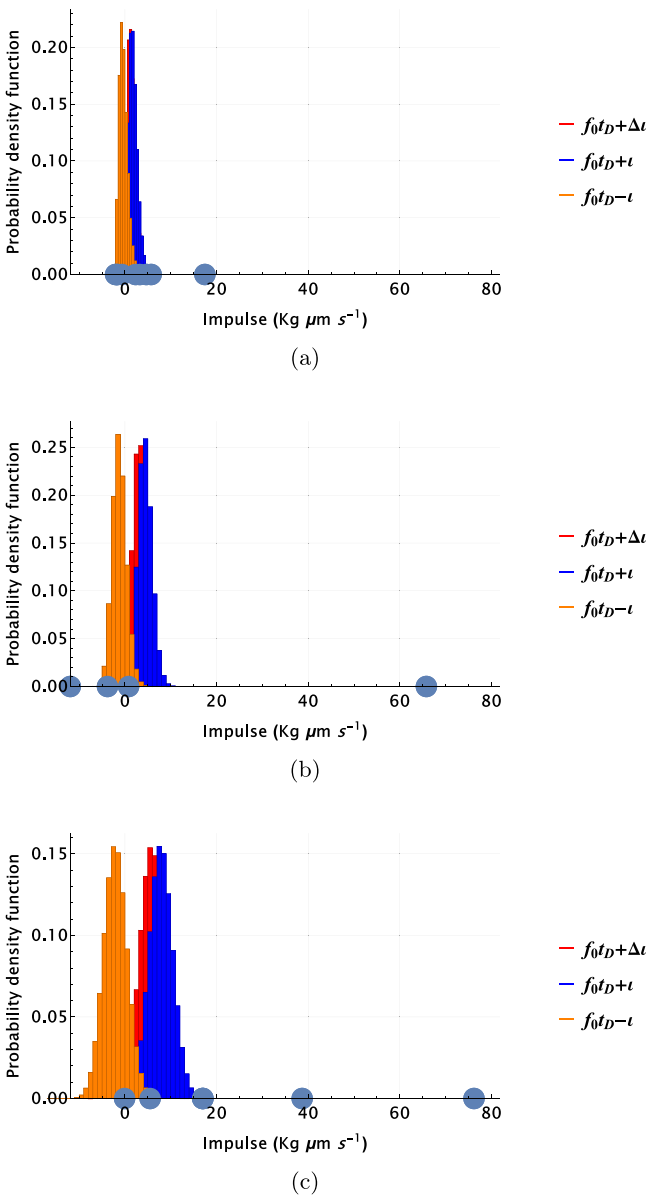

Fig. 17. Comparison between in-flight momentum $I_{z,res}$ and its ground-based predicted probability density function, assuming adhesion on both tips or one tip (Z^+ and Z^-). (a) 100 mN preload (b) 300 mN preload (c) 500 mN preload.

1. If the impacts between plungers and TM at the release are avoided, the remaining in-flight dynamics is nominal, i.e. may be explained as a combination of the effects of adhesion, time lag and residual contact preload.
2. In the nominal dynamics, the time lag between the retraction of the two tips and the residual contact preload at the release combine producing the main contribution to the momentum along the z axis.
3. The contribution of adhesion, even if present, is less critical.

The results of the ground test may be used to estimate the probability of a successful release, in the hypothesis that the GPRM mechanism for LISA is developed in order to avoid any spurious interaction between plungers and TM, i.e. according to a nominal dynamics. For the three cases of adhesive contacts addressed (both tips, only +z tip and only -z tip) the probability of a compliant momentum is calculated according to the three $PDF_{\mathrm{TM,j}}$ and are reported in Table 5. It can be

concluded that, for the LPF nominal case (i.e., 300 mN of tip preload), the TM release is expected to be successful in 99.99% of the cases.

Table 5
Probability that $I_{z,res}$ is less than the maximum available budget ($10\,\mathrm{kg\,\mu m\,s^{-1}}$, which is referred to as $I_{z,req}$) in the three cases considered. It should be noted that the release success probability exceeding 99.99% is obtained specifically under a preload condition of 300 mN, which is the LPF nominal case.

Group	$P(f_0 t_D + \Delta\iota \leq I_{z,req})$	$P(f_0 t_D - \iota \leq I_{z,req})$	$P(f_0 t_D + \iota \leq I_{z,req})$
100 mN	100.00%	100.00%	100.00%
300 mN	99.99%	100.00%	99.98%
500 mN	97.46%	100.00%	88.53%

It may be concluded that a re-design of the GPRM finalized to avoid any interaction between plungers and TM at the release can result in a nominal and compliant injection procedure.

5. Conclusions

The injection of an object into a geodesic trajectory constitutes a relevant engineering challenge to the success of a space mission. In this paper, we present the case of LISA Pathfinder, where a combined ground–flight testing approach is adopted to develop a mechanism to perform the injection of a 2 kg gold-coated test mass into a geodesic trajectory of unprecedented purity. The analysis of the in-flight behavior of the mechanism in LISA Pathfinder highlights that an anomalous dynamics occurred, affected by spurious interactions between its end effectors and the released test mass. However, subtracting these unwanted dynamical effects from the in-flight performance, it is possible to highlight that the underlying "nominal" dynamics is compatible with the ground-based tests and, above all, compliant with the design requirements. On the LISA science mission project side, this result is relevant, as it supports a mechanism development mainly focused on achieving the nominal behavior. In order to remove the spurious effects that drove the unexpected performance, the baseline for the GPRM redesign focuses on:

- increasing the clearance between the plunger and the TM. This is achieved either by integrating longer piezo-stacks or by commanding both piezo-stacks simultaneously;
- reducing plunger lateral vibrations at the tip retraction. This is accomplished by refining the manufacturing, assembly, and integration processes of the GPRM;
- reducing plunger axial vibrations at the tip retraction. This is achieved with an improved balancing of the actuation piezo-stack;
- minimizing the friction in the linear guiding system [53,54]. The reduction of the friction reduces the non-rectilinear motion of the plungers during the release procedure. The friction minimization is achieved changing the slider/roller coupling;
- integrating a more precise and accurate force sensor, allowing a finer control on the preload applied by the tip.

The combined implementation of these modifications reduces the risk of collisions between the plunger and the TM during release. Some of the proposed modifications are implemented in a breadboard model of the GPRM, which is currently being tested at the University of Trento.

CRediT authorship contribution statement

E. Dalla Ricca: Writing – review & editing, Writing – original draft, Visualization, Validation, Software, Methodology, Investigation, Formal analysis, Data curation, Conceptualization, Resources, Supervision. **D. Bortoluzzi:** Writing – review & editing, Writing – original draft, Visualization, Validation, Supervision, Resources, Project administration, Methodology, Investigation, Funding acquisition, Formal analysis, Conceptualization. **D. Vignotto:** Writing – original draft, Visualization, Validation, Software, Methodology, Formal analysis, Conceptualization. **M. Tomasi:** Visualization, Software, Investigation, Data curation. **A. Gelan:** Visualization, Software, Data curation.

Declaration of competing interest

The authors declare the following financial interests/personal relationships which may be considered as potential competing interests: Daniele Bortoluzzi reports financial support was provided by Italian Space Agency. If there are other authors, they declare that they have no known competing financial interests or personal relationships that could have appeared to influence the work reported in this paper.

Acknowledgments

The authors wish to thank the LISA Pathfinder collaboration for the support throughout this work. This research is financially supported by ESA (European Space Agency), ASI (Italian Space Agency, grant number 2017-29-H.1-2020 "Attività per la fase A della missione LISA"), INFN (National Institute for Nuclear Physics).

References

[1] P. Fortescue, G. Swinerd, J. Stark, Spacecraft Systems Engineering, John Wiley & Sons, 2011.
[2] 2026, European Cooperation for Space Standardization, https://ecss.nl/.
[3] E. Roberts, Space tribology: its role in spacecraft mechanisms, J. Phys. D: Appl. Phys. 45 (50) (2012) 503001.
[4] C.J. Dennehy, A survey of reaction wheel disturbance modeling approaches for spacecraft line-of-sight jitter performance analysis, in: Proceedings 18th European Space Mechanisms and Tribology Symposium, ESMATS, 2019.
[5] P. Touboul, B. Foulon, M. Rodrigues, J. Marque, In orbit nano-g measurements, lessons for future space missions, Aerosp. Sci. Technol. 8 (5) (2004) 431–441.
[6] L. Giulicchi, S.-F. Wu, T. Fenal, Attitude and orbit control systems for the LISA pathfinder mission, Aerosp. Sci. Technol. 24 (1) (2013) 283–294.
[7] S. Vidano, C. Novara, L. Colangelo, J. Grzymisch, The LISA DFACS: A nonlinear model for the spacecraft dynamics, Aerosp. Sci. Technol. 107 (2020) 106313.
[8] C. Reigber, P. Schwintzer, H. Lühr, et al., The CHAMP geopotential mission, Boll. Geof. Teor. Appl 40 (3–4) (1999) 285–289.
[9] A. Calabia, S. Jin, Assessment of conservative force models from GRACE accelerometers and precise orbit determination, Aerosp. Sci. Technol. 49 (2016) 80–87.
[10] D. Arnold, T. Grombein, L. Schreiter, V. Sterken, A. Jäggi, Reprocessed precise science orbits and gravity field recovery for the entire GOCE mission, J. Geod. 97 (7) (2023) 67.
[11] E. Friis-Christensen, H. Lühr, D. Knudsen, R. Haagmans, Swarm–an earth observation mission investigating geospace, Adv. Space Res. 41 (1) (2008) 210–216.
[12] C. Everitt, B. Muhlfelder, D. DeBra, B. Parkinson, J. Turneaure, A. Silbergleit, E. Acworth, M. Adams, R. Adler, W. Bencze, et al., The gravity probe b test of general relativity, Classical Quantum Gravity 32 (22) (2015) 224001.
[13] P. Touboul, G. Métris, M. Rodrigues, J. Bergé, A. Robert, Q. Baghi, Y. André, J. Bedouet, D. Boulanger, S. Bremer, et al., M I C R O S C O P E mission: Final results of the test of the equivalence principle, Phys. Rev. Lett. 129 (12) (2022) 121102.
[14] Y. Gong, J. Luo, B. Wang, Concepts and status of Chinese space gravitational wave detection projects, Nat. Astron. 5 (9) (2021) 881–889.
[15] G. Wanner, Space-based gravitational wave detection and how LISA pathfinder successfully paved the way, Nat. Phys. 15 (3) (2019) 200–202.
[16] T.E. Bell, Hearing the heavens: the cosmos is thought to be awash with gravitational waves to which humanity is, as yet, deaf. Trudy E. Bell reports on LISA, an experiment on an unprecedented scale designed to put that right, Nature 452 (7183) (2008) 18–22.
[17] R. Dolesi, D. Bortoluzzi, P. Bosetti, L. Carbone, A. Cavalleri, I. Cristofolini, M. DaLio, G. Fontana, V. Fontanari, B. Foulon, et al., Gravitational sensor for LISA and its technology demonstration mission, Classical Quantum Gravity 20 (10) (2003) S99.
[18] B. Zahnd, M. Zimmermann, R. Spörri, LISA-pathfinder cage and vent mechanism-development and qualification, in: Proceedings 15th European Space Mechanism and Tribology Symposium, ESMATS, 2013, pp. 1–7.
[19] D. Bortoluzzi, P.A. Mäusli, R. Antonello, P.M. Nellen, Modeling and identification of an electro-mechanical system: the LISA grabbing positioning and release mechanism case, Adv. Space Res. 47 (3) (2011) 453–465.

[20] E.D. Ricca, Technological heritage exploitation of the experience of the LISA Pathfinder release mechanism (Ph.D. thesis), Doctoral School in Material, Mechatronics and System Engineering, University of Trento, 2024.
[21] C.D. Grimm, C. Lange, M. Lange, O. Mierheim, L. Witte, K. Sasaki, S. Chand, E. Ksenik, J.-T. Grundmann, T.-M. Ho, et al., The MASCOT separation mechanism: A reliable, low-mass deployment system for nano-spacecraft, CEAS Space J. 12 (3) (2020) 343–365.
[22] M. Benedetti, D. Bortoluzzi, M. Da Lio, V. Fontanari, The influence of adhesion and sub-Newton pull-off forces on the release of objects in outer space, J. Tribol. 128 (4) (2006) 828–840, https://doi.org/10.1115/1.2345407.
[23] D. Bortoluzzi, D. Vignotto, E. Dalla Ricca, J. Mendes, Investigation of the in-flight anomalies of the LISA pathfinder test mass release mechanism, Adv. Space Res. 68 (6) (2021) 2600–2615.
[24] D. Bortoluzzi, M. De Cecco, S. Vitale, M. Benedetti, Dynamic measurements of impulses generated by the separation of adhered bodies under near-zero gravity conditions, Exp. Mech. 48 (6) (2008) 777–787.
[25] D. Bortoluzzi, L. Baglivo, M. Benedetti, F. Biral, P. Bosetti, A. Cavalleri, M. Da Lio, M. De Cecco, R. Dolesi, M. Lapolla, et al., LISA pathfinder test mass injection in geodesic motion: status of the on-ground testing, Classical Quantum Gravity 26 (9) (2009) 094011.
[26] M. Benedetti, D. Bortoluzzi, S. Vitale, A momentum transfer measurement technique between contacting free-falling bodies in the presence of adhesion, J. Appl. Mech. 75 (1) (2008) http://dx.doi.org/10.1115/1.2755104.
[27] M. De Cecco, D. Bortoluzzi, L. Baglino, M. Benedetti, M. Da Lio, Measurement of the momentum transferred between contacting bodies during the LISA test-mass release phase—uncertainty estimation, Measuerment Sci. Technol. 20 (2009) 055101.
[28] M. Benedetti, D. Bortoluzzi, L. Baglivo, S. Vitale, An optimal two-input approach for impulse measurements in the nanon· s range produced by contact forces, Mech. Syst. Signal Process. 25 (5) (2011) 1646–1660.
[29] D. Bortoluzzi, M. Benedetti, L. Baglivo, S. Vitale, A new perspective in adhesion science and technology: testing dynamic failure of adhesive junctions for space applications, Exp. Mech. 50 (8) (2010) 1213–1223, http://dx.doi.org/10.1007/s11340-009-9327-5.
[30] D. Bortoluzzi, M. Benedetti, J.W. Conklin, Indirect measurement of metallic adhesion force as a function of elongation under dynamic conditions, Mech. Syst. Signal Process. 38 (2) (2013) 384–398, http://dx.doi.org/10.1016/j.ymssp.2013.01.019.
[31] D. Bortoluzzi, M. Benedetti, L. Baglivo, M. De Cecco, S. Vitale, Measurement of momentum transfer due to adhesive forces: On-ground testing of in-space body injection into geodesic motion, Rev. Sci. Instrum. 82 (12) (2011) 125107, http://dx.doi.org/10.1063/1.3658479.
[32] D. Bortoluzzi, C. Zanoni, J. Conklin, On-ground testing of the role of adhesion in the LISA-pathfinder test mass injection phase, Adv. Space Res. 59 (10) (2017) 2572–2582, http://dx.doi.org/10.1016/j.asr.2017.02.030.
[33] D. Bortoluzzi, J.W. Conklin, C. Zanoni, Prediction of the LISA-pathfinder release mechanism in-flight performance, Adv. Space Res. 51 (7) (2013) 1145–1156, http://dx.doi.org/10.1016/j.asr.2012.11.001.
[34] C. Zanoni, D. Bortoluzzi, Experimental-analytical qualification of a piezoelectric mechanism for a critical space application, IEEE/ASME Trans. Mechatronics 20 (1) (2014) 427–437.
[35] D. Bortoluzzi, C. Zanoni, S. Vitale, Improvements in the measurement of metallic adhesion dynamics, Mech. Syst. Signal Process. 52 (2015) 600–613, http://dx.doi.org/10.1016/j.ymssp.2014.06.002.
[36] D. Bortoluzzi, M. Armano, H. Audley, G. Auger, J. Baird, P. Binetruy, M. Born, D. Bortoluzzi, N. Brandt, A. Bursi, et al., Injection of a body into a geodesic: Lessons learnt from the lisa pathfinder case, in: 43rd Aerospace Mechanisms Symposium, 2016.
[37] I. Koker, H. Rozemeijer, F. Stary, K. Reichenberger, Alignment and testing of the GPRM as part of the LTP caging mechanism, in: Proceedings 15th European Space Mechanisms and Tribology Symposium, ESMATS, vol. 718, 2013, p. 21.
[38] D. Bortoluzzi, A. Zambotti, N. Favia, A vibration mode-based adhesion impulse characterization technique, Mech. Syst. Signal Process. 145 (2020) 106952, http://dx.doi.org/10.1016/j.ymssp.2020.106952.
[39] D. Bortoluzzi, E. Dalla Ricca, Analytical–experimental characterization of metallic adhesion impulses, Tribol. Int. 177 (2023) 107974.
[40] E. Dalla Ricca, D. Bortoluzzi, C. Zanoni, An improved vibration multi mode-based technique for the characterization of metallic adhesion impulses, AIAA J. 62 (10) (2024) 3988–3998.
[41] F. Marzari, E. Dalla Ricca, C. Zanoni, D. Bortoluzzi, A modal-based measurement of adhesion impulses in space mechanisms, in: 2025 IEEE 12th International Workshop on Metrology for AeroSpace (MetroAeroSpace), IEEE, 2025, pp. 23–28.
[42] D. Bortoluzzi on behalf of the LISA Pathfinder Collaboration, In-flight testing of the injection of the LISA Pathfinder test mass into a geodesic, in: 12th LISA Symposium, Chicago, 2018.
[43] D. Bortoluzzi, D. Vignotto, A. Zambotti, I. Köker, H. Rozemeijer, J. Mendes, P. Sarra, A. Moroni, P. Lorenzi, Analysis of the in-flight injection of the lisa pathfinder test-mass into a geodesic, in: Proceedings 18th European Space Mechanism and Tribology Symposium, ESMATS, 2019.
[44] D. Bortoluzzi, D. Vignotto, A. Zambotti, M. Armano, H. Audley, J. Baird, P. Binetruy, M. Born, E. Castelli, A. Cavalleri, et al., In-flight testing of the injection of the LISA pathfinder test mass into a geodesic, Adv. Space Res. 67 (1) (2021) 504–520.
[45] E. Dalla Ricca, D. Bortoluzzi, D. Vignotto, Analysis and interpretation of the in-flight dynamics of a critical space mechanism, Adv. Space Res. (2024).
[46] M. Tomasi, E. Dalla Ricca, D. Vignotto, D. Bortoluzzi, Development of a dynamical model of a release mechanism for in-flight performance prediction, Adv. Space Res. 72 (11) (2023) 4950–4964.
[47] D. Vignotto, Analysis of the in-Flight Performance of a Critical Space Mechanism (Ph.D. thesis), Doctoral School in Material, Mechatronics and System Engineering, University of Trento, 2021.
[48] L. Meirovitch, Elements of vibration analysis, 1975.
[49] S.M. Kay, Fundamentals of Statistical Signal Processing: Estimation Theory, Prentice-Hall, Inc., 1993.
[50] A. Zambotti, Ground Testing and In-Flight Performance of a Space Mechanism (Ph.D. thesis), Doctoral School in Material, Mechatronics and System Engineering, University of Trento, 2019.
[51] D.C. Montgomery, G.C. Runger, Applied Statistics and Probability for Engineers, John wiley & sons, 2010.
[52] A. Papoulis, Probability and Statistics, Prentice-Hall, Inc., 1990.
[53] D. Vignotto, C. Zanoni, M. Tomasi, D. Bortoluzzi, E. Dalla Ricca, I. Pretto, P. Radaelli, The role of friction in the LISA-pathfinder release mechanism anomaly, AIAA J. 61 (12) (2023) 5232–5241.
[54] G. Agostini, M. Tomasi, F. Marzari, D. Bortoluzzi, A. Moroni, M. Grespi, R. Freddi, Delta-development of the LISA release mechanism, in: 2025 IEEE 12th International Workshop on Metrology for AeroSpace (MetroAeroSpace), IEEE, 2025, pp. 35–40.